A Predictive Modeling Tool for Damage Analysis and Design of Hydrogen Storage Composite Pressure Vessels

Ba Nghiep Nguyen[*,a], Hee Seok Roh[b], Daniel R Merkel[a], Kevin L Simmons[a]

[a]*Pacific Northwest National Laboratory, Richland, WA 99354, USA*

[b]*Argonne National Laboratory, 9700 South Cass Avenue, Argonne, IL, 60439, USA*

Abstract: In this paper, a predictive modeling tool is developed for damage analysis and design of hydrogen (H_2) storage composite pressure vessels. It integrates micromechanics of matrix cracking into a continuum damage mechanics (CDM) description for damage evolution, and three-dimensional (3D) finite element (FE) modeling of the vessel structural response. At the scale of the composite layer (mesoscale), the temperature-dependent stiffness reduction law in terms of the damage variable for transverse matrix cracking is computed using an Eshelby-Mori-Tanaka approach (EMTA) for the initial composite thermoelastic properties and a self-consistent model for the stiffness reduction as a function of the damage variable. While transverse matrix cracking obeying a damage evolution relation can progressively evolve from an initiation to a saturation state, fiber failure is predicted by a micromechanical fiber rupture criterion that accounts for the fiber strength and matrix stress that can be computed within EMTA. The implementation of this integrated multiscale modeling model into a 3D FE formulation enables damage analysis and design of H_2 storage composite pressure vessels. The developed tool is illustrated through 3D damage analyses of a cryogenically compressed H_2 storage vessel model subjected to thermomechanical loadings to investigate effects of the helical layer fiber orientation and loading scenario on damage development, vessel integrity and burst pressure.

Keywords: Hydrogen storage pressure vessel, micromechanics, continuum damage mechanics, transverse matrix cracking, fiber rupture.

[*]Corresponding author: **Ba.Nguyen@pnnl.gov**

1. Introduction

According to the United States Department of Energy (US DOE) Hydrogen and Fuel Cell Technologies Office* (DOE-HFTO), fuel-cell-powered light duty vehicles require enough hydrogen (H_2) to provide a driving range of more than 300 miles with the ability to quickly and easily refuel the vehicle. Onboard hydrogen storage capacities of 5–13 kg hydrogen will be required to meet this driving range for the full range of light-duty vehicle platforms. DOE-HFTO has set new targets for medium- and heavy-duty vehicles with range with ranges up to 750 miles, between 40 and 80 kg hydrogen of onboard hydrogen storage with refueling rates of less than 10 minutes [1-2]. Current practices that rely on compressed gas onboard storage using large-volume, high-pressure composite vessels are volumetric, gravimetric, and cost challenged for light-duty vehicles. The onboard storage for medium- and heavy-duty trucks have similar challenges to their light-duty vehicle counterparts but have other challenges such as large storage volumes that require storage packaging on the vehicle. Therefore, technological solutions aim at increased H_2 density and insulated pressure vessels may allow for the above DOE targets to be met. To this end, cryo-compressed H_2 storage pressure vessels are being considered and constitute the main motivation for our work. These pressure vessels possess a liner (metallic or polymeric) overwrapped by high-strength carbon fiber (CF)/epoxy composite layers. There is a huge challenge to design a cryo-compressed pressure vessel for sustaining thermomechanical cycling involving large temperature changes. Thermomechanical cycling induces high stresses and large stress variations in the CF/epoxy overwrap, which can in turn cause matrix cracking, fiber/matrix debonding, delamination, and fiber rupture, leading to vessel failure. Transverse matrix cracking is one of the most dangerous failure mechanisms since it can initiate even at early stages of loading and amplifies with increasing loads or number of cycles. Since cryo-compressed H_2 pressure vessels operate in cryogenic temperature ranges, particular attention is paid to this failure mechanism as the epoxy matrix becomes brittle at low temperatures and is vulnerable to cracking. It has been observed that epoxies exhibit brittle behavior with very small strain to failure at cryogenic temperatures [4-6]. Transverse matrix cracking is studied in this work within the context of cryo-compressed H_2 pressure vessels. The objective is to develop a predictive modeling tool for damage

*https://www.energy.gov/eere/fuelcells/hydrogen-storage

analysis and design of these vessels that have been considered in fuel-cell powered vehicles [7-10].

In a recent article [3], we have provided a review of models [11-19] that were developed to analyze pressure vessels. These models explored the meso-macro [11-18] or micro-meso-macro [3,19] approaches to compute the vessel macroscopic response. Models using the meso-macro approach compute the behavior of the vessel from the behavior of the composite lamina given a priori while models exploring the micro-meso-macro approach predicts the composite vessel behavior from those of the microscale constituents (i.e., fiber and matrix). In addition to these approaches, there have been micro-macro approaches [20-21] that use a reference volume element or unit cell to obtain the damage state at the constituent level to be fed into the macroscopic FE model of a pressure vessel. Nevertheless, a lot of modeling work on pressure vessels cited above applied the meso-macro approach in combination with the classical lamination theory (CLT) or a finite element (FE) method associated a failure criterion [22-24]. The use of a failure criterion requires lamina's strength data that were obtained through mechanical testing on flat specimens. This could represent a tremendous amount of efforts given temperature-dependent mechanical property data needed. In addition, as pointed out in [3], the *micro-meso-macro* approach offers a more efficient way than the meso-macro one to obtain the lamina behavior in complex laminated composite structures such as filament-wound pressure vessels for which data obtained from conventional flat specimens do not necessarily reflect actual mechanical properties of the layers in the vessels.

While continuum damage mechanics (CDM) have been significantly explored to model progressive damage in laminated composite structures [25-29], its applications to pressure vessels have still been very limited. At the time of this paper, CDM has not yet been explored in damage analysis of cryo-compressed H_2 pressure vessels undergoing thermomechanical loadings. Chapelle and Perreux [15] pioneered in CDM for H_2 pressure vessel analysis using Tsai-Wu's criterion to predict failure of the vessel laminate. Using CDM in combination with a failure criterion in FE analyses of H_2 pressure vessels was also conducted in Refs [13-14]. As pointed out in Ref. [3], according to CDM, the material damage is governed by the damage evolution law(s) according to which the damage variable(s) can evolve from an initial value to a critical (saturation) value (≤ 1) at which failure or fracture occurs [25-29]. Since failure corresponds to the critical state of damage for the associated damage variable, a general failure or a given mode of failure can be predicted

within the CDM formalism without the need of using a classical failure criterion like Tsai-Wu's or Hashin's criterion, etc. that requires the composite layer's strength data.

The present paper also explores the multiscale (micro-meso-macro) modeling approach developed in Refs [3, 19] for pressure vessels as schematically depicted in Fig. 1. The differences between the model developed in this paper with those in our previous work [3, 19] and the studies by other authors [11-21] are that this paper develops and uses a CDM formulation of transverse matrix cracking accounting for thermomechanical effects on the composite response in three-dimensional (3D) analyses of a cryo-compressed H_2 pressure vessel. At the micro and meso scales, the composite stiffness tensor affected by transverse matrix cracking is computed using an Eshelby-Mori-Tanaka approach (EMTA) for the initial composite thermoelastic properties combined with a self-consistent model for the stiffness reduction as a function of the damage variable associated with this mechanism [30]. Transverse matrix cracking that obeys a damage evolution relation within the framework of continuum damage mechanics (CDM) [25-29] can progressively evolve from an initiation to a saturation state. Composite failure by fiber rupture during vessel loading is predicted by a micromechanical fiber failure criterion that accounts for the fiber strength and matrix stress [3]. The direct interaction between matrix cracking and fiber failure is explicitly captured in this criterion. By involving micromechanics of transverse matrix cracking and fiber failure into a CDM constitutive formulation, the model directly captures the physics of defects in the prediction of the vessel response.

To achieve a predictive modeling tool for damage analysis and design of H_2 storage composite pressure vessels, this integrated multiscale modeling model has been implemented in the Abaqus FE code by means of user subroutines. In this paper we illustrate its useful applications through 3D damage analyses of a cryogenically compressed H_2 storage vessel model subjected to thermomechanical loadings to investigate effects of the helical layer fiber orientation and loading scenario on damage development, vessel integrity and burst pressure. The core structure of the paper is as follows. After the Introduction (Section 1), Section 2 discusses transverse matrix cracking in laminated composites and the application of the self-consistent model to obtain the stiffness reduction law. The constitutive relations and damage evolution law that integrate the stiffness reduction law are described in Section 3. Section 4 focuses on the materials and input data needed for damage FE analyses using this predictive modeling tool. Section 5 illustrates the application of the predictive tool through damage analyses of a Type-3 cryo-compressed pressure

vessel made of a steel liner and a CF/epoxy overwrap. Two loading scenarios and two different angles for the helical layers in the vessel's cylindrical part were considered to determine their effects on damage development, structural integrity and burst pressure of the vessel. The conclusions from this work are drawn in Section 6.

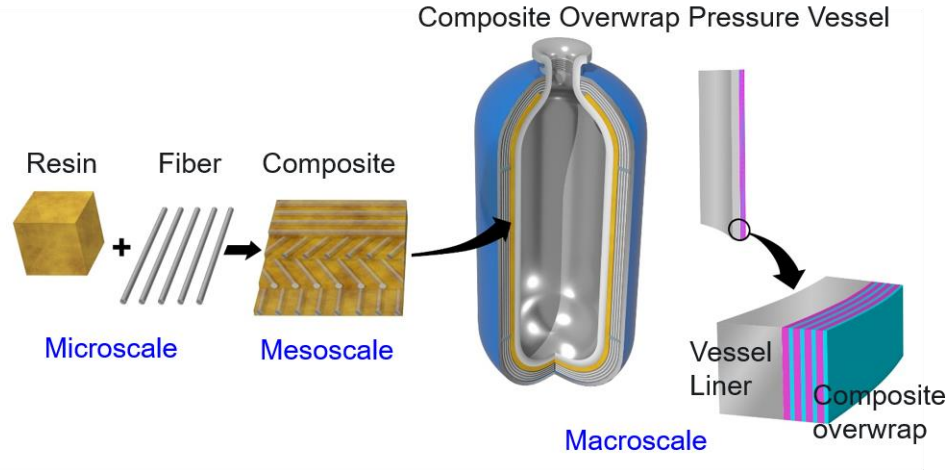

Fig. 1. Schematic of the multiscale mechanistic approach to analyze H_2 storage composite pressure vessels.

2. Transverse matrix cracking in laminated composites

There is a very large body of literature studying transverse matrix cracking in laminated fiber polymer composite flat specimens e.g., [28-34]. This damage mechanism can occur early in these composites even at low load levels. Transverse matrix cracking also occurs in non-flat specimens such as pressure vessels. Subjected to thermomechanical loading, cryo-compressed H_2 storage pressure vessels may experience high stresses that can trigger transverse matrix cracking in their laminated CF/epoxy overwrap. Once amplified, matrix cracking can lead to delamination and fiber rupture causing vessel failure. This paper explores an established model of transverse matrix cracking [30] to numerically determine its effects on the composite stiffness. The goal is to establish a sound stiffness reduction law for the composite to be later integrated into a mechanistic continuum damage model implemented in a finite element (FE) code for damage analysis of pressure vessels.

Fig. 2 shows a two-dimensional (2D) schematic of a basic [0°/90°/0°] cross-layer laminate for the numerical characterization of transverse matrix cracking. Although transverse cracking can

occur in laminated composites with other layer fiber orientations, a typical [0°/90°/0°] laminate is chosen for the characterization purpose since this mechanism almost exclusively occurs in such a laminate subjected to tensile loading before its final failure. Fig. 2(a) depicts the transverse cracks in the 90° layer of a [0°/90°/0°] laminate. These cracks often initiate from preexisting microvoids or from resin-rich locations in the 90° layer. The crack distribution is generally not uniform. Commonly, the nonuniform distribution of cracks can be replaced by a statistically uniform one shown in Fig. 2(b) so that a mean crack spacing L can be defined such that the crack density (number of crack per unit length) is given by $1/L$.

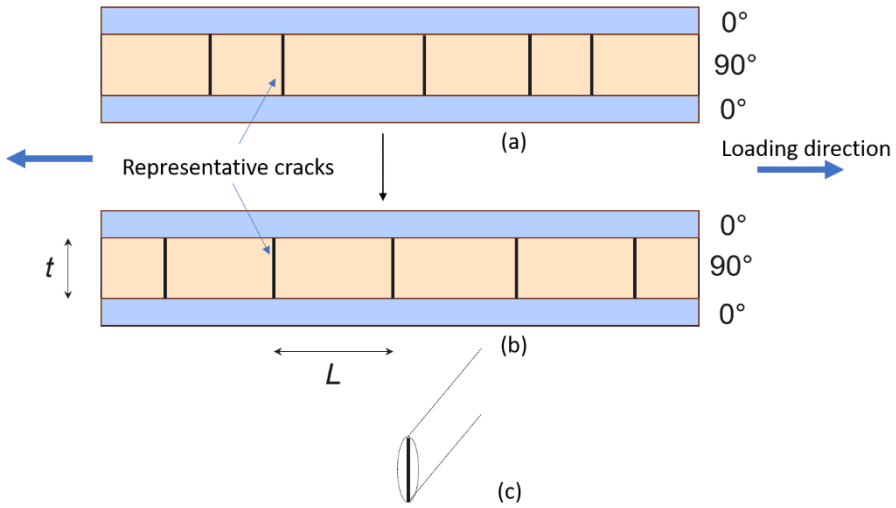

Fig. 2. (a) A 2D schematic of a [0°/90°/0°] laminate containing transverse cracks in its 90° layer, (b) the nonuniform crack distribution is replaced by a uniform one; and (c) concept of degenerescence of a cylindrical inclusion into a crack used by Laws et al. [30]. In this schematic, fibers in the 0° layers align with the loading direction.

Next, the Laws et al. self-consistent model [30] is used to compute the reduction of the composite stiffness as a function of the crack density. Laws et al. used the solution of an inclusion problem for an elliptic cylinder in an anisotropic elastic medium to obtain the expressions for the stiffness and compliance tensors as a function of the damage variable α, defined as $\alpha = t/L$ with t being the cracked layer thickness. These authors modeled a transverse crack as the degenerescence of a cylindrical inclusion of infinite length when its elliptical cross section smaller (semi-minor) axis tends to zero (Fig. 2(c)). According to this model, the fourth-order stiffness **C** and compliance **S** tensors of a cracked composite are given by:

$$\mathbf{C} = \mathbf{C}^0 - \frac{1}{4}\pi\alpha\mathbf{C}^0\mathbf{\Lambda}\mathbf{C} \quad (1)$$

$$\mathbf{S} = \mathbf{S}^0 + \frac{1}{4}\pi\alpha\mathbf{\Lambda} \quad (2)$$

where the superscript "0" denotes the initial uncracked state. $\mathbf{\Lambda}$ is a fourth-order tensor that depends on the components of the compliance tensor. Solving systems (1-2) numerically yields **C** and **S** for a given value of the damage variable α, which can vary from 0 (the uncracked state) to a crack saturation state corresponding to $\alpha = \alpha_c$.

Fig. 3 illustrates the stiffness reduction predicted by the Laws et al. model in terms of the normalized stiffness versus the damage variable α for a typical CF/epoxy composite having 0.6 fiber volume fraction. The constituent elastic properties were taken from [19]. Transverse cracking affects the composite stiffness very significantly. The stiffness tensor components that are the most affected by this damage mechanism are C_{22} and C_{12}, and C_{23} along with C_{66}, which corresponds to the shear modulus G_{12} (with "1" being the fiber direction and "2" transverse to the fiber direction). Note that this model yields $C_{22} = C_{12} = C_{23}$ and C_{55} is not affected by transverse cracking.

Nguyen [28-29] has shown that the stiffness reduction predicted by Laws et al.'s model [30] for a fiber polymer composite system as a function of damage variable α can be fitted by exponential expressions of the form used by Renard et al. [27]:

$$C_{ij}(T, \alpha) = C_{ij}^0(T) \exp\left[-k_{ij}(T)\,\alpha\right] \quad (3)$$

with $C_{ij}^0(T)$ being the temperature (T)-dependent stiffness tensor of the composite at the initial undamaged state. $k_{ij}(T)$ are the temperature-dependent stiffness reduction parameters that can be identified by a fitting procedure [28]. The tensorial contracted indices are used in Eq. (3), and no summation rule is applied to indices i and j. In this work $C_{ij}^0(T)$ is computed by an EMTA model from the constituent elastic properties [35-37]. Note that it is necessary to determine $k_{ij}(T)$ for an internal cracked layer (inside the laminate), the corresponding values for an external cracked layer are twice the values for the internal layers [27-28].

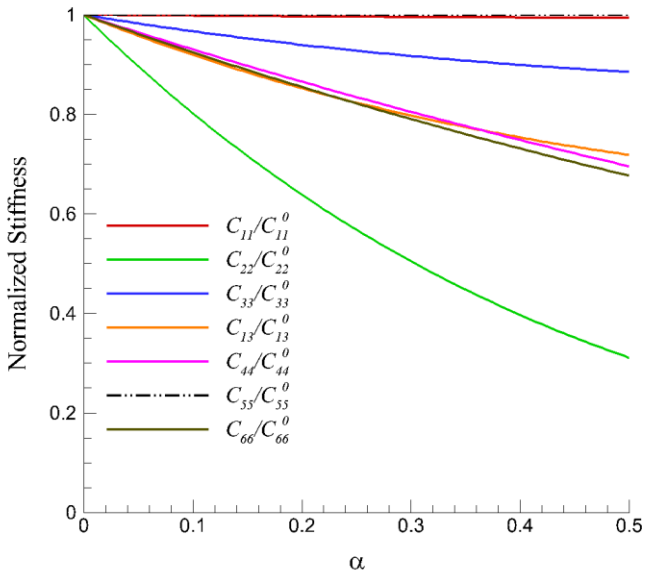

Fig. 3. Predicted stiffness reduction due to transverse matrix cracking vs. damage variable $\alpha = t/L$ for a CF/epoxy composite.

To assess the prediction of stiffness reduction by Laws et al.'s model, we have used this model in the analyses of various cross-layer laminates studied in Grove et al. [38] that provides the constituent ply elastic properties and experimental crack density data for those laminates made of CF/epoxy composites. In these analyses, after application of the Laws et al.'s model to the cracked layer, the lamination theory was applied to compute the elastic properties of the as-formed laminates. Fig. 4 reports the analysis results for the normalized laminate modulus E_{xx}/E_{xx}^0 versus crack density that agree reasonably well with the experimental data by Grove et al. [38] for various cross-layer laminates. The laminate *x*-direction is the loading direction orthogonal to the transverse cracks. These results confirm the accuracy of the EMTA and self-consistent micromechanics in the computation of the composite stiffness affected by transverse matrix cracking.

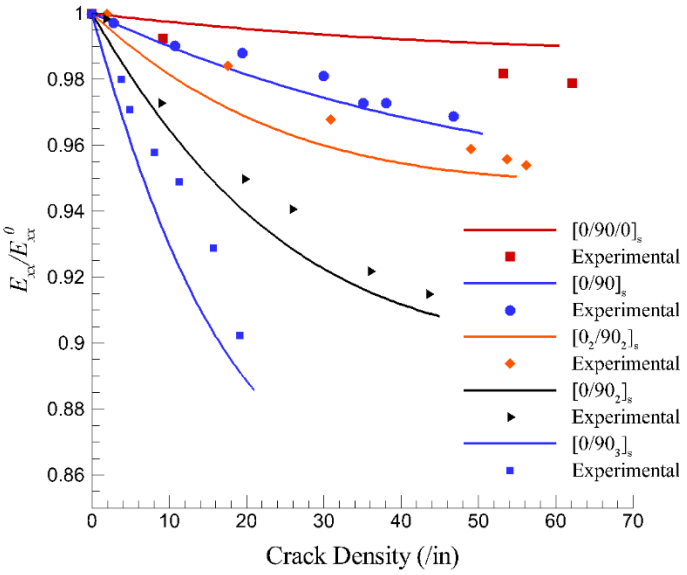

Figure 4. Normalized axial modulus reduction predicted for various cross-ply laminates compared to Grove et al.'s data [38].

3. Constitutive modeling

A multiscale mechanistic damage approach has been developed and implemented in a 3D FE formulation for H_2 pressure vessel analyses. This approach incorporates Laws et al.'s model [30] and EMTA [35-37] in the continuum damage mechanics (CDM) formulation used by Renard et al. [27] and generalized to 3D finite element analysis by Nguyen [28-29]. In this work, the approach is further extended starting from an initial work by Nguyen and Fleury [39] to incorporate the temperature-dependent material properties and model parameters as well as thermal stresses that are essential for thermomechanical analyses of H_2 pressure vessels. The thermodynamic potential for an elastic damage composite is taken as the density of deformation energy expressed in terms of temperature T, mechanical strain ε_i and the damage variable α:

$$\Phi\,(T, \varepsilon_i, \alpha) = \frac{1}{2}\, C_{ij}(T, \alpha)\varepsilon_i\varepsilon_j \qquad (4)$$

where the tensorial contracted indices are used, and the stiffness tensor of the composite as a function of α is given by Eq. (3).

The mechanical strains are given in terms of the total ($\varepsilon_i^{\mathrm{t}}$) and thermal ($\varepsilon_i^{\mathrm{th}}$) strains as:

$$\varepsilon_i = \varepsilon_i^{\mathrm{t}} - \varepsilon_i^{\mathrm{th}} = \varepsilon_i^{\mathrm{t}} - \int_{T_0}^{T} \beta_i(T)dT \quad (5)$$

where $\beta_i(T)$ are the composite coefficients of thermal expansion (CTEs), and T_0 is a reference temperature. The CTEs for the composite ply can be computed for a given temperature from those of the constituents using an EMTA formulation for thermal expansion such as the one developed by Takao and Taya [40].

From the potential (4) and considering uniform temperature distribution, the constitutive relations and thermodynamic force (damage driving force) associated with the damage variable at a given temperature are obtained as:

$$\sigma_i = \frac{\partial \Phi(T,\varepsilon_i,\alpha)}{\partial \varepsilon_i} = C_{ij}(T,\alpha)\varepsilon_j \quad (6)$$

$$F(\alpha,T) = \frac{\partial \Phi(T,\varepsilon_i,\alpha)}{\partial \alpha} = \frac{1}{2}\frac{\partial C_{ij}(T,\alpha)}{\partial \alpha}\varepsilon_i\varepsilon_j \quad (7)$$

For a constant temperature distribution, the Clausius-Duhem's inequality that expresses the total dissipation is [39]:

$$-F(\varepsilon_i,\alpha,T)\dot{\alpha} - \frac{\mathbf{q}.\nabla T}{T} \geq 0 \quad (8)$$

where $\mathbf{q}$ is the heat flux vector. Inequality (8) includes two terms. The first term defines the intrinsic dissipation, and the second represents thermal dissipation. In this work, the uncoupling between intrinsic and thermal dissipations is considered leading to

$$-F(\varepsilon_i,\alpha,T)\dot{\alpha} \geq 0 \quad (9)$$

and

$$-\frac{\mathbf{q}.\nabla T}{T} \geq 0 \quad (10)$$

Inequality (9) implies that the damage process is irreversible, thus α can never decrease. Inequality (10) the work thermally dissipated per unit volume must be positive.

The damage evolution law for α that expresses the increase of damage as a function of strain and strain increments at a given temperature is obtained using the same thermodynamic framework described in [27-29] that consider a damage criterion dependent on a damage threshold function $F_{\mathrm{c}}(\alpha,T)$, $f = F - F_{\mathrm{c}}$, the consistency condition $f = 0, df = 0$, and the Second Law of

Thermodynamics that dictates the energy dissipation and irreversible character of damage (Inequality (9)):

$$d\alpha = -\frac{\frac{\partial C_{ij}(T,\alpha)}{\partial \alpha}\varepsilon_i d\varepsilon_j}{\frac{1}{2}\frac{\partial^2 C_{ij}(T,\alpha)}{\partial \alpha^2}\varepsilon_i\varepsilon_j - \frac{\partial F_c(T,\alpha)}{\partial \alpha}} \tag{11}$$

In the context of pressure vessel applications, the damage evolution law (11) is strictly rigorous when applied to compute the damage increments in the composite overwrap during autofrettage or pressure loading steps at given temperatures. During uniform cooling, Eq. (11) can still be applied under *quasi static* conditions for which the temperature evolves from an initial state to a final one by a succession of equilibrium permanent states.

The material damage due to microcracking under tensile or combined stress states leads to an increase in damage according to Eq. (8). A purely compressive state of stresses is assumed not to activate damage or not further induce damage from an initial state. The damage threshold function $F_c(\alpha, T)$ can be identified using the material stress-train data and Eq. (7) by prescribing $F_c(\alpha, T) = F$. Damage evolves according to Eq. (11) until reaching a critical or saturation state corresponding to a saturation value of α: $\alpha = \alpha_c$ that will lead the composite to fracture (total failure) by a combination of matrix cracking, delamination and fiber rupture. To determine how close matrix cracking is to the saturation state (given by α_c), we define a matrix failure indicator as α/α_c. While delamination is not treated in this paper, total failure of the composite layer caused by fiber rupture is predicted by a micromechanical criterion:

$$\frac{|\sigma_{11}|}{\sigma_{11}^f} = \frac{|\sigma_{11}|}{\mu_f\sigma_f + (1-\mu_f)\,\sigma_m} = 1 \tag{12}$$

where σ_{11} is the composite fiber direction stress, μ_f and σ_f denote the fiber volume fraction and fiber strength, respectively; and σ_m is the matrix equivalent stress. The composite strength in the fiber direction σ_{11}^f is computed in a similar fashion to the method used in Ref. [3]. However, in the combined CDM-micromechanics formulation used in the present paper, σ_m in the expression of σ_{11}^f is influenced by matrix cracking and is computed within the EMTA framework as follows. First, the matrix strain increment $\Delta\boldsymbol{\varepsilon}_m$ is computed in terms of the overall composite strain increment $\Delta\boldsymbol{\varepsilon}$ as:

$$\Delta\boldsymbol{\varepsilon}_m = \mathbf{A}_m : \Delta\boldsymbol{\varepsilon} \tag{13}$$

where the matrix strain concentration tensor $\mathbf{A}_{\mathrm{m}}$ is related to $\mathbf{A}_{\mathrm{f}}$, the fiber strain concentration tensor as

$$(1-\mu_{\mathrm{f}})\mathbf{A}_{\mathrm{m}} + \mu_{\mathrm{f}}\mathbf{A}_{\mathrm{f}} = \mathbf{I} \tag{14}$$

where $\mathbf{A}_{\mathrm{f}} = \mathbf{T}\colon[(1-\mu_{\mathrm{f}})\mathbf{I} + \mu_{\mathrm{f}}\mathbf{T}]^{-1}$ with $\mathbf{T} = [\mathbf{I} + \mathbf{S}\colon\mathbf{C}_{\mathrm{m}}^{-1}\colon(\mathbf{C}_{\mathrm{f}} - \mathbf{C}_{\mathrm{m}}(T,\alpha)]^{-1}$. $\mathbf{C}_{\mathrm{f}}$ and $\mathbf{C}_{\mathrm{m}}(T,\alpha)$ are the stiffness tensors of the fiber and matrix, and $\mathbf{I}$ the fourth-order identity tensor. Next, the matrix stress increment is computed by

$$\Delta\boldsymbol{\sigma}_{\mathrm{m}} = \mathbf{C}_{\mathrm{m}}(T,\alpha)\colon\Delta\boldsymbol{\varepsilon}_{\mathrm{m}} \tag{15}$$

$\mathbf{C}_{\mathrm{m}}(T,\alpha)$ can be computed from Eqs. (1) and (2) using the stiffness and compliance tensors of the matrix material and its components can be fitted by the exponential expressions similar to Eq. (3).

$$C_{ij}^{\mathrm{m}}(T,\alpha) = C_{ij}^{\mathrm{m},0}(T)\exp\left[-k_{ij}^{\mathrm{m}}(T)\,\alpha\right] \tag{16}$$

where k_{ij}^{m} are stiffness reduction parameters for the matrix material. Computation of matrix stress increment (15) allows the matrix stresses and matrix equivalent stress to be updated at each increment to evaluate fiber failure criterion (12). The composite is predicted to fail completely if criterion (12) is equal to 1. Fracture leading to initiation and propagation of a macroscopic crack is captured in the model by a vanishing element method [41, 28-29].

4. Materials and Model Input Data

Continuous CF reinforced epoxy composites have been considered as prime composite materials for the overwraps of H_2 storage pressure vessels. For the sake of illustration for the predictive modeling tool using the mechanistic damage model presented in Sections 3 and 4, we have considered typical published thermomechanical properties for CF/epoxy composite as well as for constituent CFs and epoxies to establish a data set for the FE analyses of a cryo-compressed H_2 storage pressure vessel model presented in Section 5. The multiscale modeling approach depicted in Fig. 1 requires the constituent thermoelastic properties as input data. First, we started with the T300/914 CF/epoxy composite studied in [27,32] where the unidirectional (UD) ply's elastic properties and crack density versus applied stress on various laminates made of this composite are given at RT. The EMTA reverse engineering [19] was then applied to identify constituent elastic properties from those of the UD ply given in [32]. Table 1 gives the constituent

elastic properties (in the material orthotropic axes) determined by this procedure for the T300/914 composite lamina with 0.57 fiber volume fraction. T300 CF's strength (= 3530 MPa) used in the analyses was from Torayca T300 data sheet.

CF's elastic properties and longitudinal CTE ($\sim -4.1 \times 10^{-7}$/K) are reasonably assumed to be constant in the 50–293 K temperature range [3]. However, the variation of the CF's transverse CTE with temperature was accounted for in the analyses using the data in Ref. [42]. The elastic modulus of the epoxy matrix was assumed to vary linearly from the value at RT (3.6 GPa) to the value at 77 K (6 GPa). In the absence of the CTE data for the 914-epoxy matrix in the [77, 293 K] range, the measured CTEs of an in-house epoxy given in [3] and shown in Fig. 5 were used in the analyses. Figure 5 also gives the temperature-dependent transverse CTE for CF based on [42].

Table 1. Elastic properties of constituents and UD T300/914 with 0.57 fiber volume fraction.

	T300 Fiber	**914 Epoxy Matrix**	**T300/914 (EMTA)**	**T300/914 [32]**
E_{11} (GPa)	230.	3.6	132.7	130.
$E_{22} = E_{33}$ (GPa)	30.		9.96	10.
$G_{12} = G_{13}$ (GPa)	16.		5.05	5.
G_{23} (GPa)	11.54		4.21	---
$\nu_{12} = \nu_{13}$	0.25	0.4	0.31	0.35
ν_{23}	0.3		0.54	---

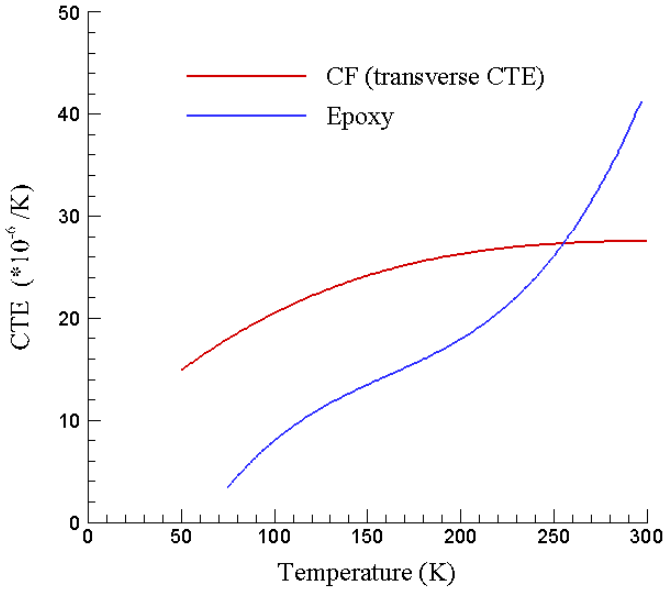

Figure 5. Transverse CTE of CF based on Ref. [42] and CTE of an epoxy conceived in-house as a function of temperature.

For the application of the damage model at cryogenic temperatures, the crack density versus applied stress data from CF/epoxy cross-ply laminates as a function of temperature in the cryogenic temperature range relevant to H_2 storage vessel applications are needed to identify the damage model parameters. While significant crack density data for these laminates tested at RT can be found in literature, such data including those for the T300/914 considered in this paper are not available or are very limited at cryogenic temperatures [43-44]. In the following, we have used the crack density data for the T300/914 CF/epoxy known at RT [32] and considered a crack density evolution at 77 K that represents a significantly stronger composite at this temperature. Such a cracking behavior is illustrated in Fig. 6(a). On this figure, for a same value of the applied stress above the onset cracking level, the crack density at 77 K is lower than the value at RT. The model parameters for the damage threshold function were then identified using the crack density data at RT and 77 K considering the same crack density at saturation (~1.2 mm^{-1}). Subsequently, the model can predict any crack density evolution in the [77, 298 K] range (e.g., 150 K) using the parameters interpolated between RT and 77 K.

The experimental crack density evolutions obtained from the tensile tests on $[0°_2/90°_2]_s$ and $[90°_2/0°_2]_s$ laminates show different cracking behaviors [27,32]. In these laminates the 90° cracked

layer is internal and external, respectively. An internal cracked layer constraint between two adjacent layers exhibits significantly higher crack density than an external layer that has a free surface. The layer position effect was discussed in [27-28]. The mechanistic damage model can capture this difference in the cracking behavior that depends on the layer position in addition to the other key governing parameters such as the layer thickness and fiber orientation. Fig. 6(b) shows the experimental crack density data for a T300/914 $[90°_2/0°_2]_s$ laminate at RT [32] based on which the damage threshold function parameters for an external cracked layer were identified at RT. Similar consideration for a stronger composite at 77 K can be made for the cracking behavior of an external layer allowing the determination of these parameters at 77 K for this layer, and subsequently, using the parameters interpolated between RT and 77 K, the model can predict any crack density evolution in the [77, 298 K] range (e.g., 150 K) for an external cracked layer.

Limited crack density data reported for other CF/epoxy systems at cryogenic temperatures show faster crack developments at cryogenic temperatures than at RT [43-44]. This is a particular concern for CF composites processed with some common epoxies for room or higher temperature applications that exhibit high strength at RT but are not designed for composite structures operating at low temperatures. To remedy this issue, our current effort is also devoted to design epoxies that can exhibit significantly higher strength at cryogenic temperatures to reduce transverse matrix cracking. Fig. 7 shows such a behavior for the stress/strain curves obtained at 233 K and 20 K while the 90 K curve presents much lower strength and would lead to fast crack development if this behavior is produced in a composite. Our resin material study of the curing process and cross-link densities to achieve high-strength epoxies at cryogenic temperatures is ongoing at this time and will be discussed in a separate paper.

The damage threshold function numerically determined at RT and 77 K can be fitted by the following function [45]:

$$F_c(\alpha, T) = -b(T)\,\mathrm{Exp}\left(\frac{\ln\left[-\ln\left(1-\frac{\alpha}{c(T)}\right)\right]}{a(T)}\right) \quad (13)$$

where $a(T)$, $b(T)$, and $c(T)$ are the material parameters that depend on temperature and layer position in the layup. Table 2 provides these coefficients at RT and 77 K for the internal and external layers made of T300/914 considered in this work.

Table 2. Coefficients of the damage threshold function

Parameters (T300/914)	RT	77 K
a (internal)	2.2	2.2
b (internal)	0.52	1.04
c (internal)	0.6	0.6
a (external)	4.2	4.2
b (external)	1.28	2.0
c (external)	0.11	0.11

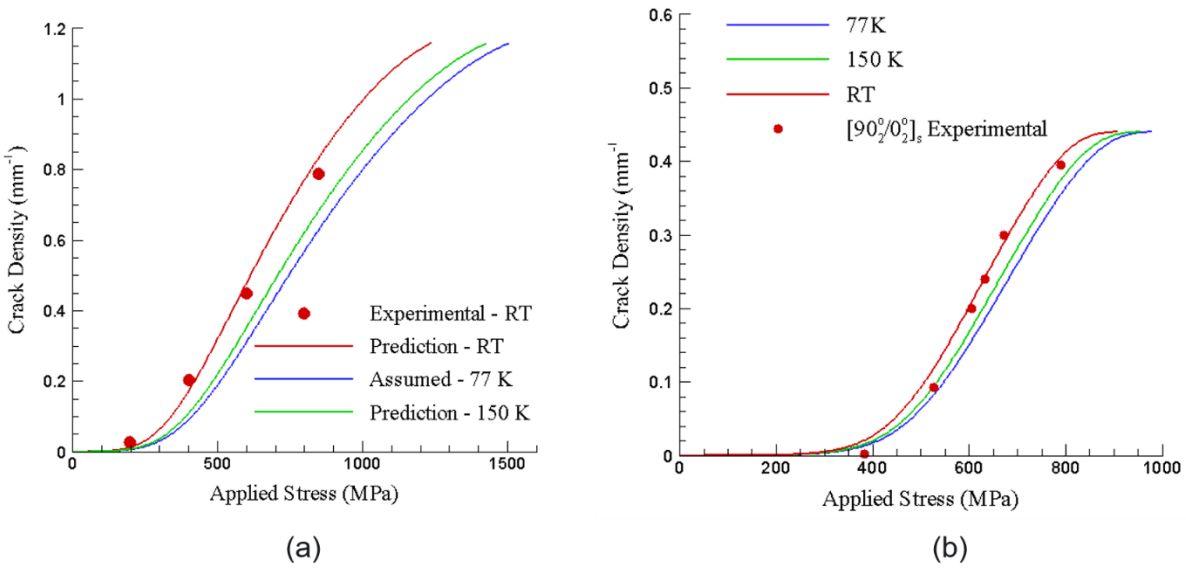

Figure 6. Crack density versus applied stress for the T300/914 (a) $[0°_2/90°_2]_s$ and (b) $[90°_2/0°_2]_s$ laminates used to determine damage model parameters in the [77, 298 K] range.

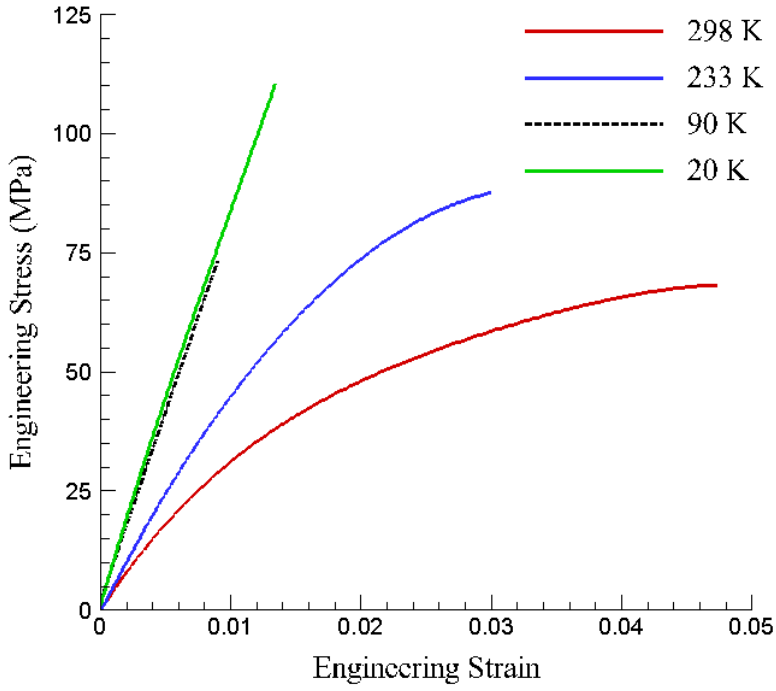

Figure 7. Experimental stress-strain curves for an in-house processed epoxy as a function of temperature.

The mechanical properties including temperature-dependent stress-strain data for steel 304 used for the liner were from Ref. [46]. A standard elastic-plastic constitutive model in Abaqus was used to describe the behavior the liner.

5. Results and Discussion

5.1 Finite element model and loading scenarios

A 3D FE model for a half of a Type-3 cryo-compressed pressure vessel (Fig. 8) made of a steel liner and a CF/epoxy overwrap formed by the hoop and helical layers was developed for the study in this work. The vessel was created with 3D linear brick elements. The FE mesh shown in Fig. 7 contains 267360 elements. Symmetric displacement boundary conditions are applied on the model bottom while the liner's inner surface is subjected to internal pressure that is controlled through the prescribed loading scenario. The liner's inner diameter and wall thickness are 196 mm and 2mm, respectively. The composite overwrap consists of 90° hoop and ±20° helical layers stacked up according to the sequence: liner/±20°/90°/±20°/90°. The hoop and helical layers have the same thickness (3 mm). The hoop layers reinforce the vessel along the circumferential direction and the

helical layers reinforce the tank not only along the axial direction but also the vessel's dome section. Since the internal pressure of Type-3 cryo-compressed vessels is mostly carried by the composite layers, the total thickness of these layers was preliminarily estimated to carry the operating pressure of 50 MPa with a safety factor of 2.25. When the helical layer passes through the dome, the thickness of the helical layer changes as the fiber angle changes due to the change in the radius of the dome. A bandwidth of 25 mm was used to create filament windings over the liner. One element was allocated per winding layer, and a total of seven elements are used in the thickness direction of the vessel. More details of the layup procedure are described in Ref [47], and in this study, changes of fiber angle and layer thickness in the dome were considered in our FE model by using the Abaqus Wound Composite Modeler (WCM).

Damage analyses of this vessel model subjected to two different thermomechanical loading scenarios were performed using the developed mechanistic damage model (Sec. 3 and 4) implemented in Abaqus. The CF/epoxy for the composite overwrap is the T300/914 discussed in the previous section. In the first and second applications, we investigated the helical layer fiber orientation effects by performing comparative analyses considering another layup for the overwrap in which the helical layers in the cylindrical body were oriented at ±15°. Both pressure vessels with the ±20° and ±15° helical layers were subjected to loading scenario 1 including an autofrettage at RT with 70-MPa autofrettage pressure, a uniform cooling to 77 K and a pressure loading at 77 K until causing complete failure of the vessels. In the third application, the vessel with the ±20° helical layers was subjected to loading scenario 2 with an autofrettage applied at RT using the same autofrettage pressure, but this vessel was uniformly cooled to 110 K before the internal pressure was ramped up at this temperature until causing its bursting.

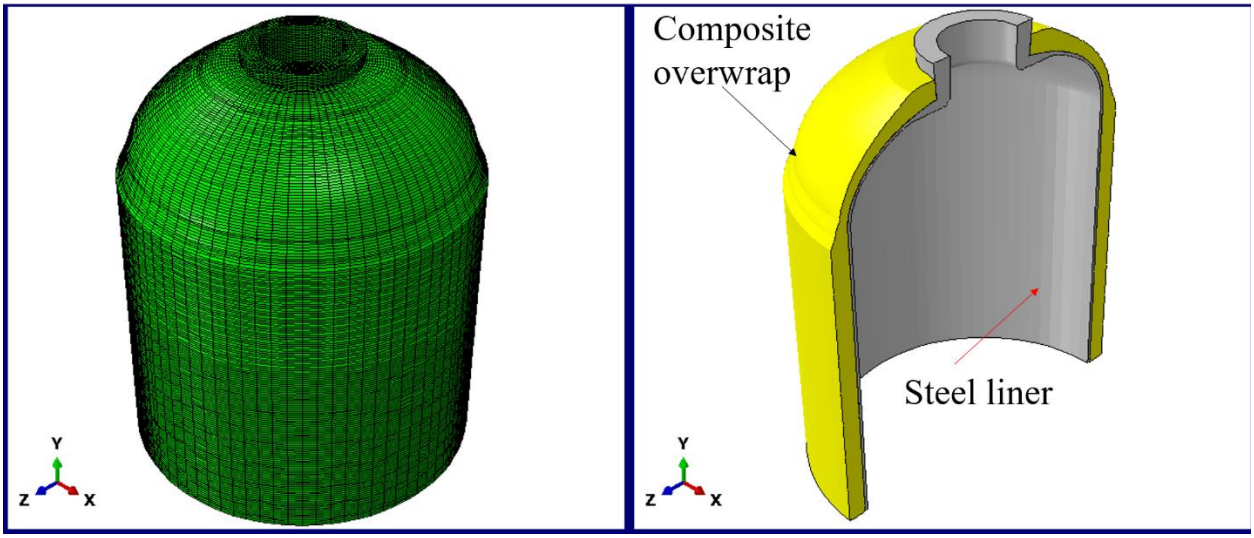

406

407 **Figure 8.** The 3D FE model developed for FE damage analyses and a vertical cross section
408 showing the vessel interior including the steel liner and composite overwrap.

409

410 *5.2 Effects of helical layer fiber orientation*

411 Fig. 9(a) presents the contour of matrix cracking damage of the vessel with ±20° helical layers
412 after cooling to 77 K. The matrix failure indicator is defined by the current value of damage
413 variable normalized by its value at transverse crack saturation (=α/α_c). Cooling to 77 K after
414 autofrettage at 70 MPa pressure caused some localized damage near the top of the dome at the
415 location in contact with the liner (Fig. 9(a)). The junction region between the dome and the
416 cylindrical body of the vessel also experienced minor damage. The localized damages were caused
417 by concentrations of transverse stress σ_{22} in these regions as shown in Fig. 9(b) that provides the
418 contour of transverse stress σ_{22} in the vessel overwrap at the end of cooling to 77 K.

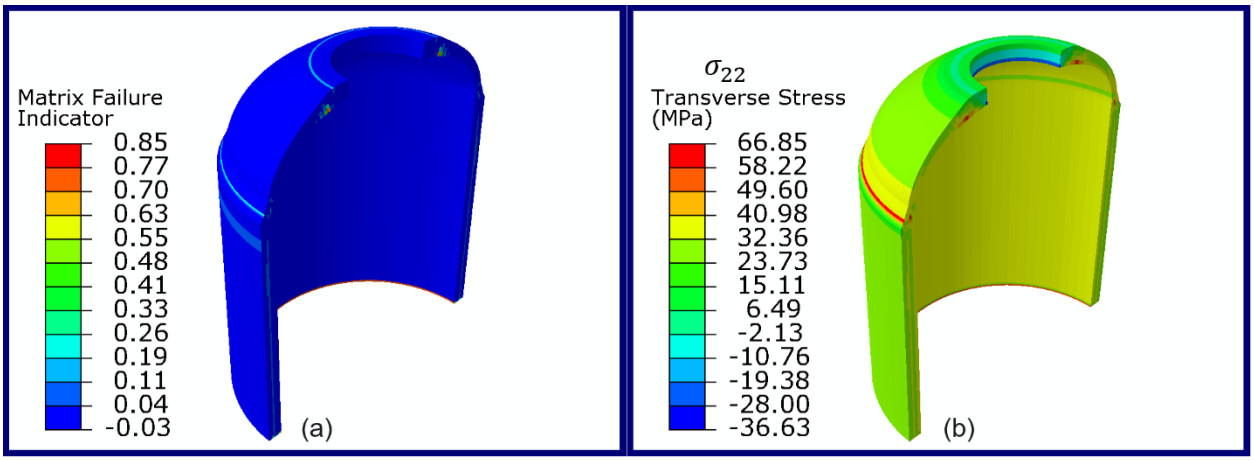

Figure 9. Contours of (a) matrix failure indicator and (b) transverse stress σ_{22} at the end of cooling to 77 K.

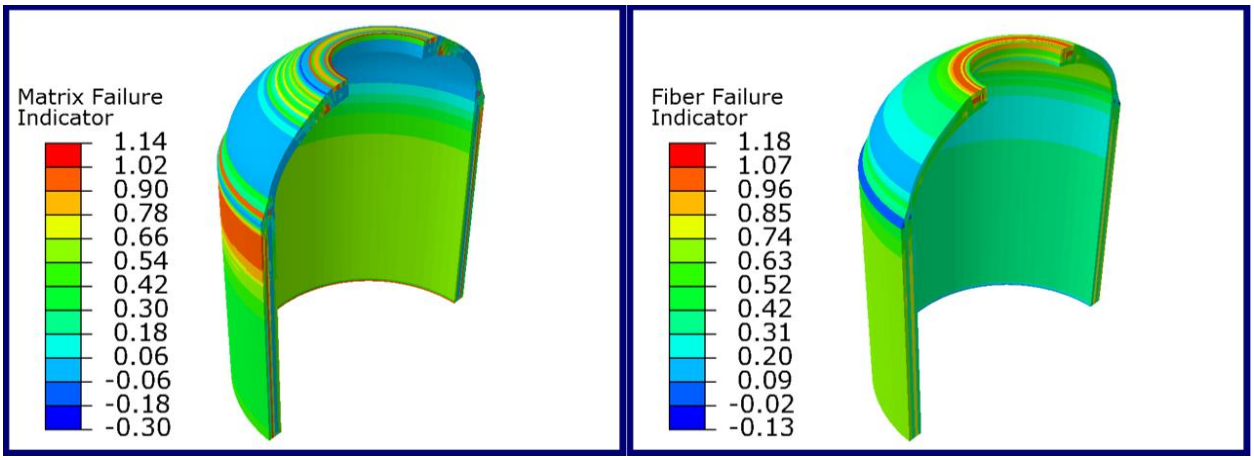

Figure 10. Contours of (a) matrix failure and (b) fiber failure indicators in the vessel with ±20° helical layers at 119.3 MPa pressure and 77 K.

During the bursting step, the internal pressure was increased incrementally until causing total failure of the vessel. Total failure is predicted to occur if the liner is ruptured or if the vessel suffers either from matrix cracking through all the layers of its overwrap, or fiber failure happens in any part of the overwrap. Figs 10(a) and 10(b) show the distributions of matrix and fiber failure indicators at 119.3 MPa pressure. The vessel overwrap has completely failed at this pressure level due to fiber failure in the region at the top of the dome Fig. 10(b). The model also predicted extensive matrix damage in different regions of the overwrap as illustrated in Fig. 10(a), but the vessel bursting was mainly caused by fiber failure in this case.

In the second analysis, we considered a vessel similar to the previous one, but the orientations of its overwrap's helical layers were oriented at ±15°. The fiber orientations in the dome remained unchanged. Figs 11(a) and 11(b) show the contours of matrix and fiber failure indicators in this vessel at 119.5 MPa pressure. This pressure level has caused complete failure of the vessel due to fiber breakage in the region at the top of the dome Fig. 11(b). In addition, intensive matrix cracking damage has also been found in different layers and sections of the vessel (Fig. 11(a)). Comparing Fig. 11(a) to Fig. 10(a) and Fig. 11(b) to Fig. 10(b) reveals that at practically the same bursting pressure (~119.3 MPa), the vessel with ±15° helical layers has experienced significantly more matrix damage than the vessel with ±20° helical layers while the contours of fiber failure indicator are quite similar. These findings show that the vessel layup can be tailored in terms of fiber orientation to reduce matrix cracking damage for improving the vessel integrity.

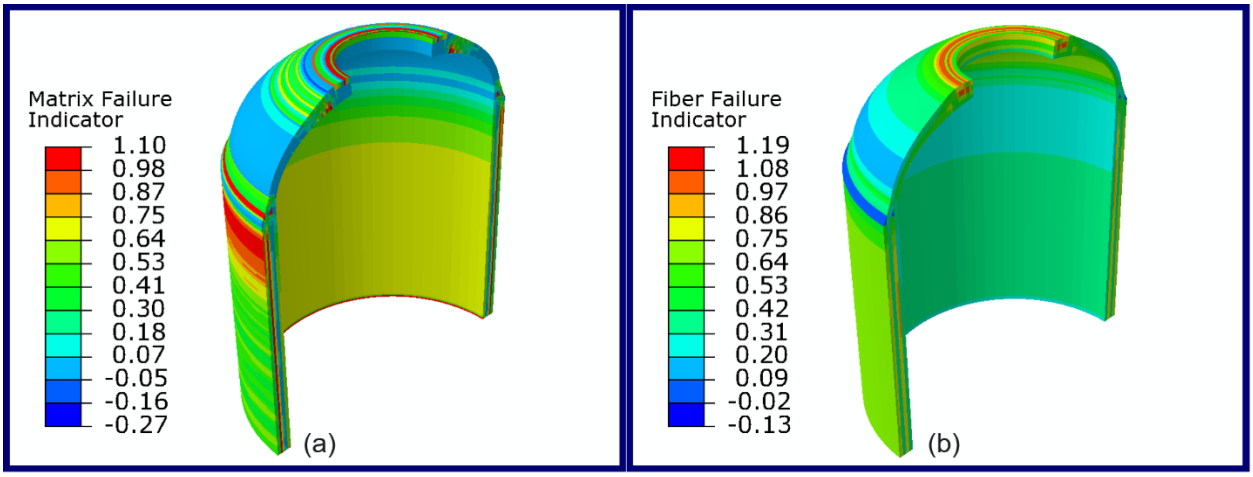

Figure 11. Contours of (a) matrix failure and (b) fiber failure indicators in the vessel with ±15° helical layers at 119.5 MPa pressure and 77 K.

5.3 Loading scenario effects

In this application, we examined the effects of cooling and pressuring temperature on the vessel integrity. The vessel with ±20° helical layers was subjected to loading scenario 2 that also includes an autofrettage at RT but after it was cooled to 110 K, the internal pressure was ramped up at this temperature until causing its bursting. We then compare the damage distribution in this case to the previous cases involving this vessel model subjected to loading scenario 1 discussed in the previous section. Figs 12(a) and 12(b) show the contours of matrix and fiber failure indicators in this vessel at 117 MPa pressure. Failure of this vessel occurred at 117 MPa due to a combination

of severe matrix cracking in different layers and sections (Fig. 12(a)) with fiber breakage at the top of the dome (Fig. 12(b)). The contour of matrix failure indicator presented in Fig. 12(a) is quite similar to the contour shown in Fig. 11(a) for the vessel with ±15° helical layers bursting at 119.5 MPa pressure and 77 K. In both cases, substantial matrix cracking in different parts of the cylindrical body and dome combined with fiber failure at the top of dome has caused bursting of the vessel. In the vessel pressured at 110 K, more matrix damage has been predicted at final failure (Fig. 12(a)).

To have a more quantitative examination of the effects of the helical layer orientation and of the pressurizing temperature, Figs 13(a) and 13(b) report the evolutions of the matrix failure criterion as a function of the applied pressure at two different locations named A and B in the vessel. Location A is situated inside an internal helical layer near the junction between the dome and cylindrical part, and Location B is away from the junction region and situated in the helical layer in contact with the liner.

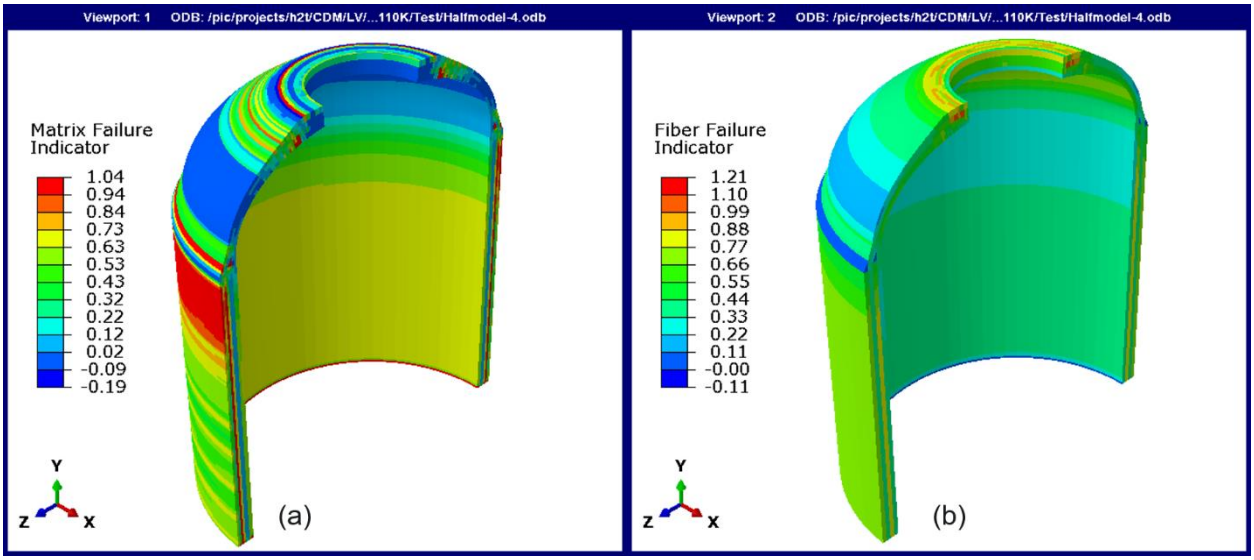

Figure 12. Contours of (a) matrix failure and (b) fiber failure indicators in the vessel with ±20° helical layers at 117 MPa pressure and 110 K.

Fig. 13(a) shows that matrix damage at Location A of the vessel with ±20° helical layers pressurized at 77 K is significantly lower than the damage at the same location in this vessel pressurized at 110 K. Changing the helical layer fiber orientation from ±20° to ±15° has resulted in very little change in damage evolution at 77 K. However, for Location B in contact with the liner and away from the junction area, matrix cracking is more important for the vessel with ±20°

helical layers pressurized at 110 K than the same vessel pressurized at 77 K (Fig. 13(b)). Modifying the layer fiber orientation from ±20° to ±15° has also worsened matrix damage at this location. Comparing Fig. 10(a) to Figs 11(a) and 12(a) shows that the 20° helical layer in contact with the liner pressurized at 77 K generally exhibits significantly less damage than the same layer pressurized at 110 K or the 15° layer pressurized at 77 K.

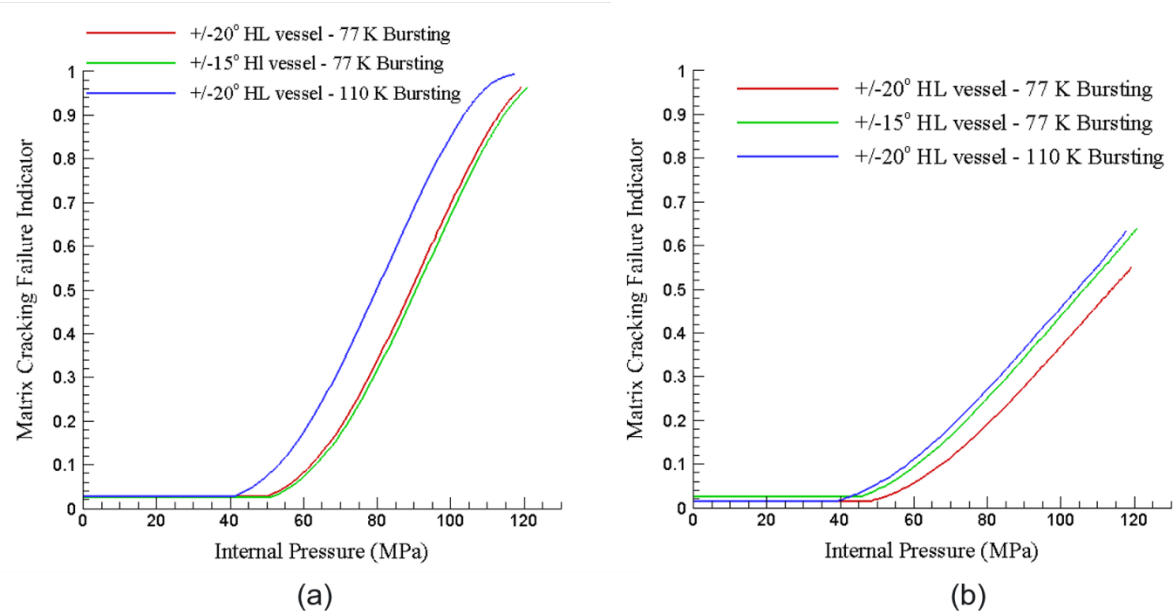

Figure 13. Matrix cracking failure indicator versus internal pressure at (a) Location A inside an internal helical layer near the junction between the dome and cylindrical part, and (b) Location B away from the junction region and situated in the helical layer in contact with the liner.

6. Conclusions

A predictive modeling tool for damage analysis and design of composite H_2 storage composite pressure vessels was developed in this paper. The predictive tool uses a mechanistic multiscale modeling approach to the composite constitutive behavior affected by progressive damage by transverse matrix cracking. As this is a micro-meso-macro approach, it requires the constituent thermoelastic properties and fiber strength in addition to crack density versus applied stress data on laminates as model inputs. Fiber failure is predicted by a micromechanical criterion that accounts for the fiber strength and matrix stress. Thus, the model explicitly accounts for the interaction between transverse matrix cracking and fiber breakage. By incorporating the

micromechanics of matrix cracking into a CDM description for damage evolution, and 3D FE modeling of the vessel structural response, this approach enables damage analysis and design of H_2 pressure vessels in terms of material selection, composite overwrap layup and loading scenario. We have conducted 3D FE analyses of a Type-3 cryo-compressed H_2 storage pressure vessel model and have examined the effects of helical fiber orientation and loading scenario on the resulting damage development and structural integrity of the vessel. The following conclusions are drawn from the analyses:

- Considering a stronger crack resistance behavior at temperatures lower than RT, the model predictions show the benefits for pressurizing at cryogenic temperatures, a necessary condition for operating cryo-compressed H_2 pressure vessels.
- It is essential to achieve stronger composite at cryogenic temperatures through optimized processing and constituent material selections. High-strength CF helps increase the burst pressure as matrix cracking can still occur until crack saturation before fiber failure.
- Fiber orientation has an important effect on matrix cracking development. The predictive tool using such as a mechanistic approach to damage is very helpful to tailor the composite layup in terms of fiber orientations in different sections of the vessel. For instance, our future work will focus on not only improving the layup for the vessel's cylindrical body but also the design of its dome where local fiber orientations are complex in order to minimize early matrix cracking occurring in this part.
- Combining fiber orientation optimization through vessel design with adequate loading scenarios could mitigate or reduce the risk of vessel failure, particularly during thermomechanical cycling.

Acknowledgements

This work was fully supported by the U.S. Department of Energy (US DOE), Office of Energy Efficiency and Renewable Energy (EERE), Hydrogen Fuel Cell Technologies Office (HFTO) under Contract No. DE-AC05-76RL01830 and Contract No. DE-AC02-06CH11357. Pacific Northwest National Laboratory is operated by Battelle Memorial Institute for the US DOE under contract DE-AC05-76RL01830. Argonne National Laboratory, a US DOE Office of Science laboratory, is operated by UChicago Argonne, LLC, under Contract No. DE-AC02-06CH11357.

Disclaimers

The views and opinions of the authors expressed herein do not necessarily state or reflect those of the United States Government or any agency thereof. Neither the United States Government nor any agency thereof, nor any of their employees, makes any warranty, expressed or implied, or assumes any legal liability or responsibility for the accuracy, completeness, or usefulness of any information, apparatus, product, or process disclosed, or represents that its use would not infringe privately owned rights.

References

[1] J Marcinkoski, R Vijayagopal, J Adams, B James, J Kopasz, R Ahluwalia. Hydrogen Class 8 Long Haul Truck Targets: DOE Hydrogen and Fuel Cells Program Record 19006. October 31, 2019

[2] J Adams. DOE H2 Heavy Duty Truck Targets, Compressed Gas Storage for Medium and Heavy Duty Transportation Workshop. Lemont, IL Jan 21, 2020

[3] BN Nguyen, DR Merkel, KI Johnson, DW Gotthold, KL Simmons, and HS Roh, 2019. "Modeling the Effects of Loading Scenario and Thermal Expansion Coefficient on Potential Failure of Cryo-compressed Hydrogen Vessels," International Journal of Hydrogen Energy, 45(2020) 24883-24894.

[4] Z-K Chen, G Yang, J-P Yang, S-Y Fu, L Ye, Y-G Huang. Simultaneously increasing cryogenic strength, ductility and impact resistance of epoxy resins modified by n-butyl glycidyl ether. Polymer 2009; 50:1316–1323.

[5] Q Feng, J Yang, Y Liu, H Xiao, S Fu. Simultaneously enhanced cryogenic tensile strength, ductility and impact resistance of epoxy resins by polyethylene glycol. J. Mater. Sci. Technol. 2014; 30(1):90–96.

[6] LM Soffer, R Molho. Mechanical properties of epoxy resins and glass/epoxy composites at cryogenic temperatures. J. Macromol. Sci. - Part B (Physics) 1967; B1(4):709–739.

[7] RK Ahluwalia, TQ Hua, J-K Peng, S Lasher, K McKenney, J Sinha, M Gardiner. Technical assessment of cryo-compressed hydrogen storage tank systems for automotive applications. Int. J. Hydrogen Energy 2010; 35:4171–4184.

553 [8] DJ Durbin, C Malardier-Jugroot. Review of hydrogen storage techniques for on board vehicle
554 applications. Int. J. Hydrogen Energy 2013; 38:14595–14617.

555 [9] RK Ahluwalia, JK Peng, HS Roh, TQ Hua, C Houchins, BD James. Supercritical cryo-
556 compressed hydrogen storage for fuel cell electric buses. Int. J. Hydrogen Energy 2018; 43:10215–
557 10231.

558 [10] J Moreno-Blanco, G Petitpas, F Espinosa-Loza, F Elizalde-Blancas, J Martinez-Frias, SM
559 Aceves. The storage performance of automotive cryo-compressed hydrogen vessels. Int. J.
560 Hydrogen Energy 2019; 44:16841–16851.

561 [11] JM Lifshitz, H Dayan. Filament-wound pressure vessel with thick metal liner. Compos.
562 Struct. 1995; 32:313–323.

563 [12] D-S Son, J-H Hong, S-H Chang. Determination of the autofrettage pressure and estimation of
564 material failures of a Type III hydrogen pressure vessel by using finite element analysis. Int. J.
565 Hydrogen Energy. 2012; 37:12771-12781.

566 [13] PF Liu, LJ Xing, JY Zheng. Failure analysis of carbon fiber/epoxy composite cylindrical
567 laminates using explicit finite element method. Composites: Part B 2014; 56:54-61.

568 [14] L Wang, C Zheng, H Luo, S Wei, Z Wei. Continuum damage modeling and progressive
569 failure analysis of carbon fiber/epoxy composite pressure vessel. Composite Structures 2015;
570 134:475-482.

571 [15] D Chapelle, D Perreux. Optimal design of a Type 3 hydrogen vessel: Part I - Analytic
572 modelling of the cylindrical section. Int. J. Hydrogen Energy 2006; 31:627–638.

573 [16] B Magneville, B Gentilleau, S. Villalonga, F Nony, H. Galiano. Modeling, parameters
574 identification and experimental validation of composite materials behavior law used in 700 bar
575 type IV hydrogen high pressure storage vessel. Int. J. Hydrogen Energy 2015; 40:13193-13205.

576 [17] D Leh, B Magneville, P Saffre, P Francescato, R Arrieux, S Villalonga. Optimisation of 700
577 bar type IV hydrogen pressure vessel considering composite damage and dome multi-sequencing.
578 Int. J. Hydrogen Energy 2015; 40:13215-13230.

579 [18] HS Roh, TQ Hua, RK Ahluwalia. Optimization of carbon fiber usage in Type 4 hydrogen
580 storage tanks for fuel cell automobiles. Int. J. Hydrogen Energy 2013; 12795-12802.

[19] BN Nguyen, KL Simmons. A multiscale modeling approach to analyze filament-wound composite pressure vessels. J. Compos. Mater. 2012; 47(17): 2113–2123.

[20] L Wang, C Zheng, S Wei, Z Wei. Micromechanics-based progressive failure analysis of carbon fiber/epoxy composite vessel under combined internal pressure and thermomechanical loading. Composites Part B. 2016; 89:77-84.

[21] S Lin, L Yang, H Xu, Xi Jia, X Yang, L Zu. Progressive damage analysis for multiscale modelling of composite pressure vessels based on Puck failure criterion. Composite Structures. 2021; 255: 113046.

[22] R Hill. A theory of the yielding and plastic flow of anisotropic metals. Proc. R. Soc. London 1948; A193:281-297.

[23] SW Tsai, EM Wu EM. A general theory of strength for anisotropic materials. J. Compos. Mater. 1971; 5:58–80.

[24] Z. Hashin. Failure criteria for unidirectional fiber composites. J. Appl. Mech. 1980; 47(2):329-34.

[25] J Lemaitre, in Continuum Damage Mechanics of Materials and Structures, O Allix and F Hild, Editors. 2002, Elsevier Science Ltd: Oxford, UK. p. 235-258.

[26] P Ladeveze P, E LeDantec E. Damage modelling of the elementary ply for laminated composites. Composites Sci. & Technol 1992; 43:257-267.

[27] J Renard, J-P Favre, T Jeggy. Influence of Transverse Cracking on Ply Behavior: Introduction of a Characteristic Damage Variable. Composites Science and Technology 1993, 46:29-37.

[28] BN Nguyen. Three-Dimensional Modeling of Damage in Laminated Composites Containing A Central Hole. Journal of Composite Materials 1997, 31(17):1672-1693.

[29] BN Nguyen. Damage Modeling of Laminated Composites by the Use of Multilayer Volume Elements. Composites Science and Technology 1998, 58(6):891-905.

[30] N Laws, GJ Dvorak, and M Hejazi. Stiffness Changes in Unidirectional Composites Caused by Crack Systems. Mechanics of Materials 1983, 2:123-137.

[31] N Laws, GJ Dvorak. Progressive Transverse Cracking in Composite Laminates. Journal of Composite Materials 1988, 22: 900-915.

[32] A Thionnet, J Renard. Meso-macro Approach to Transverse Cracking in Laminated Composites Using Talreja's Model. Composites Engineering 1993, 3(9):851-871.

[33] M Herráez, D Mora, F Naya, CS Lopes, C González, J LLorca. Transverse cracking of cross-ply laminates: A computational micromechanics perspective. Composites Science and Technology 110 (2015) 196–204.

[34] MM Moure, SK García-Castillo, S Sánchez-Sáez, E Barbero, EJ Barbero. Matrix cracking evolution in open-hole laminates subjected to thermomechanical loads. Composite Structures 183 (2018) 510–520.

[35] JD Eshelby. The Determination of the Elastic Field of an Ellipsoidal Inclusion, and Related Problems. Proceedings of the Royal Society of London A: Mathematical, Physical and Engineering Sciences 1957; 241:376-396.

[36] T Mori, K Tanaka. Average Stress in Matrix and Average Elastic Energy of Materials with Misfitting Inclusions. Acta Metallurgica 1973; 21(5):571-574.

[37] Y Benveniste. A new approach to the application of Mori-Tanaka's theory in composite materials. Mechanics of Materials 1987; 6:147-157.

[38] SE Groves, CE Harris, AL Highsmith, DH Allen, RG Norvell, 1987. “An Experimental and Analytical Treatment of Matrix Cracking in Cross-Ply Laminates. Experimental Mechanics 1987; 27:73–79.

[39] BN Nguyen, C. Fleury. Damage Modeling of Laminated Composites. In: Computational Plasticity Fundamentals and Applications – Part 2, DRJ Owen, E Onate, E. Hinton, Eds., pp. 1220-1228. CIMNE, Barcelona, 1997.

[40] Y Takao, M Taya. Thermal Expansion Coefficients and Thermal Stresses in an Aligned Short Fiber Composite with Application to a Short Carbon Fiber/Aluminum. ASME Journal of Applied Mechanics 1985; 52:806-810.

[41] V Tvergaard. Influence of Void Nucleation on Ductile Shear Fracture at A Free Surface. Journal of the Mechanics and Physics of Solids 1982; 30(6): 399-425.

[42] MG Huson. High-performance pitch-based carbon fibers. In: Structure and Properties of High-Performance Fibers; Woodhead Publishing Series in Textiles, 2017, Pages 31–78.

[43] P Lundmark, J Varna. Damage evolution and characterization of crack types in CF/EP laminates loaded at low temperatures. Engineering Fracture Mechanics 2008; 75:2631–2641.

[44] T Briand, C Bois, J-C Wahl, E Le Goff, F Lavelle. Effect of ply thickness and temperature on transverse cracking process in composite laminates. In: Proceedings of International Conference on Composite Materials (ICCM22), 2019, Page 358–366, Engineers Australia, Melbourne.

[45] A Thionnet. Prévision d'endommagement sous chargements quasi-statiques et cycliques des structures composites stratifiée. Ph.D. Thesis, University of Paris 6, France, 1991.

[46] C Zheng and W Yu. Effect of low-temperature on mechanical behavior for an AISI 304 austenitic stainless steel. Materials Science and Engineering A 2018; 710: 359–365.

[47] ST Peters, ed. *Composite filament winding*. ASM International, 2011.